Photocatalytic H_2 Evolution

Zitierweise:
Internationale Ausgabe: doi.org/10.1002/anie.202301239
Deutsche Ausgabe: doi.org/10.1002/ange.202301239

Cd/Pt Precursor Solution for Solar H_2 Production and in situ Photochemical Synthesis of Pt Single-atom Decorated CdS Nanoparticles

Pankaj Sharma, Monika Sharma, Malcolm Dearg, Martin Wilding, Thomas J. A. Slater, and C. Richard A. Catlow**

Abstract: Despite extensive efforts to develop high-performance H_2 evolution catalysts, this remains a major challenge. Here, we demonstrate the use of Cd/Pt precursor solutions for significant photocatalytic H_2 production (154.7 mmol g^{-1} h^{-1}), removing the need for a pre-synthesized photocatalyst. In addition, we also report simultaneous in situ synthesis of Pt single-atoms anchored CdS nanoparticles (Pt_{SA}-CdS_{IS}) during photo-irradiation. The highly dispersed in situ incorporation of extensive Pt single atoms on CdS_{IS} enables the enhancement of active sites and suppresses charge recombination, which results in exceptionally high solar-to-hydrogen conversion efficiency of ≈1 % and an apparent quantum yield of over 91 % (365 nm) for H_2 production. Our work not only provides a promising strategy for maximising H_2 production efficiency but also provides a green process for H_2 production and the synthesis of highly photoactive Pt_{SA}-CdS_{IS} nanoparticles.

Introduction

Solar energy may be stored chemically as well as electrically.[1–4] Harvesting solar energy in H_2 production will play an essential role in solving the global energy crisis;[5] and since the first report of photocatalytic hydrogen generation by Fujishima and Honda,[6] solar-to-hydrogen energy conversion using photocatalysts has attracted great attention. Recently, H_2 production using a simple particulate photochemical system has shown great potential to achieve techno-economic viability.[7,8] For any particulate photochemical system, an efficient photocatalyst is the key feature which determines the efficiency, scalability, and cost-competitiveness of the system. However, the design of an efficient photocatalyst can be challenging,[7,9–16] both regarding the synthesis methods and the role of co-catalysts. In most previous studies,[7,10,17–24] photocatalyst synthesis protocols involved solvothermal, hydrothermal, and organic solution methods followed by multiple steps including co-catalyst loading, surface shielding, conjugation, and hybridisation. In contrast to this requirement for a pre-synthesized photocatalyst, the direct use of a photoactive reaction solution for solar H_2 production mitigates the use of multi-step synthesis methods, high-cost organic solvents, sophisticated reaction setup, additional thermal treatments and co-catalyst loading. From the perspective of practical feasibility and environmental impact, the elimination of separate synthesis steps for any photocatalyst would be very desirable.

In this paper, we report effective solar H_2 production (154.7 mmol g^{-1} h^{-1} from Cd-Pt_2-SSs suspension) by direct solar irradiation of an aqueous suspension of Cd (cadmium nitrate) and Pt (chloroplatinic acid) metal precursors in sodium sulphide (Na_2S, 0.25 M) + sodium sulphite (Na_2SO_3, 0.35 M) solution (SSs), termed as Cd_x-Pt_y-SSs. Importantly, the direct use of a precursor suspension, without using any complex photocatalyst synthesis process and organic solvents, outperforms most of the earlier reported photocatalysts for H_2 production for particulate systems that we will show later in this paper. Furthermore, the simultaneous in situ formation of Pt single-atoms anchored CdS nanoparticles (Pt_{SA}-CdS_{IS}) shows the efficacy of the strategy (Scheme 1). Thus, we demonstrate a promising, environmentally benign, and cost-effective strategy for efficient H_2 production, as well as for the synthesis of metal-semi-

[*] Dr. P. Sharma, Dr. M. Dearg, Dr. M. Wilding, Dr. T. J. A. Slater, Prof. C. R. A. Catlow
School of Chemistry, Cardiff University
Cardiff CF10 3AT (UK)
E-mail: sharmap14@cardiff.ac.uk
catlowr@cardiff.ac.uk
Dr. P. Sharma, Dr. M. Wilding, Prof. C. R. A. Catlow
UK Catalysis Hub, Research Complex at Harwell, Rutherford Appleton Laboratory
Harwell, OX11 0FA (UK)
Dr. M. Sharma
Department of Chemistry, Kurukshetra University
Kurukshetra 136119 (India)
Prof. C. R. A. Catlow
Department of Chemistry, University College London
London WC1 HOAJ (UK)

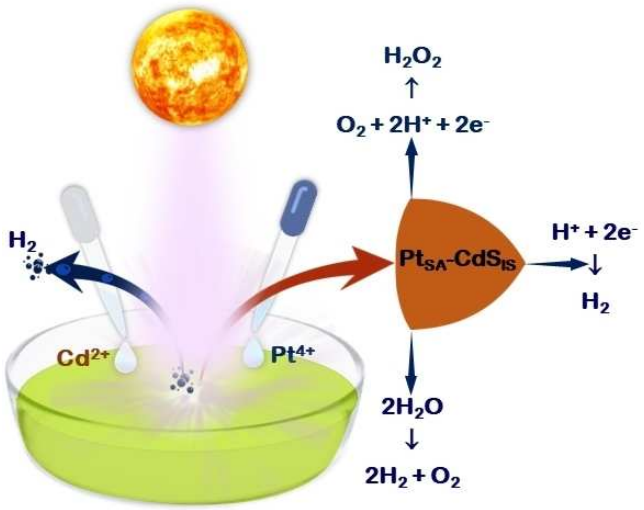

Scheme 1. Cooperative coupling of solar H_2 generation and in situ synthesis of Pt single-atom anchored CdS_{IS} nanoparticles (Pt_{SA}-CdS_{IS}) during photoirradiation. Schematic illustration highlighting the concurrent H_2 production and synthesis of Pt_{SA}-CdS_{IS} semiconductors in a single photoinduced reaction system.

conductor heterostructures suitable for photochemical, and possible other applications.

Results and Discussion

First, we tested the efficiency of the photoactive Cd_x-Pt_y-SSs reaction suspension, obtained by simple mixing of cadmium nitrate and chloroplatinic acid (Figure S1), for H_2 production under UV/Visible light illumination by using a continuous flow reaction setup connected to an online gas chromatograph (Figure S2). To study the synergistic effect of the presence of both metals in the suspension, the photoactivity of single metal precursor suspensions (Cd-SSs and Pt-SSs) were both examined (Figure S3). Next, the photoactivity of the reaction suspensions containing both the metal precursors (Cd_x-Pt_y-SSs, x = 1 mg in 15 mL SSs, y = 0.5 to 8.0 wt.% of x) was analysed to determine the optimal amount of Pt, while keeping the amount of Cd constant in the suspension (Figure 1a). It was observed that the addition of Pt to the Cd-SSs suspension increases the H_2 production rate (Figures 1a and Figure S4). The presence of 2.0 wt.% Pt in the reaction suspension (Cd-Pt_2-SSs) showed a 4.7 fold increase (154.7 mmol g^{-1} h^{-1}) in the H_2 production rate compared to Cd-SSs suspension. A further increase in Pt to 4 wt.% (Cd-Pt_4-SSs) resulted in a maximum H_2 production rate of 166.7 mmol g^{-1} h^{-1}, whereas a decrease in H_2 production rate was observed for a reaction suspension containing 8 wt.% Pt (Cd-Pt_8-SSs) (Figure 1a and Figure S4).

The Cd-SSs reaction suspension showed a high H_2 production rate (32.9 mmol g^{-1} h^{-1}) but the addition of Pt further increased the rate of H_2 production. We chose 2 wt.% Pt as the optimized Pt amount in suspension because the increase in H_2 production above 2 wt.% Pt is relatively small (< 10 %) and Pt use should be minimized to provide low-cost H_2 production. Furthermore, Figure S5 shows the effect of the Cd content in the reaction suspension with 2 wt.% Pt (Cd_x-Pt_2-SSs, x = 0.5, 1.0 and 2.0 mg) on the H_2 production rate. Overall, 1 mg Cd to 15 mL of SSs and the addition of 2 wt.% Pt (Cd-Pt_2-SSs) is considered the optimal reaction suspension for the present study.

Solar H_2 production of reaction suspensions of Cd-Pt_2-SSs and Cd-SSs under UV/Visible light, measured using the continuous flow system, are illustrated in Figure 1b. The results obtained were compared with the H_2 production photoactivity of commercial CdS_c and 2 wt.% Pt loaded commercial CdS_c (Pt@CdS_c) photocatalysts. The Cd-SSs and Cd-Pt_2-SSs exhibited remarkably high H_2 production rates of 32.9 and 154.7 mmol g^{-1} h^{-1}, respectively (Figure 1b). In contrast, the commercial CdS_c and Pt@CdS_c produced very small amounts of H_2 that remain undetectable (Figure 1b) in the continuous flow system used. Therefore, to estimate the H_2 production from commercial CdS_c and Pt@CdS_c, an air-tight cylindrical quartz reactor capped with rubber septa (Figure S1) was used under the same conditions by dispersing 1 mg of the photocatalyst in 15 mL SSs containing 2 wt.% Pt (relative to Cd metal). Before light irradiation, the precursor suspension was degassed by continuous purging of high purity Ar gas for 30 min in the dark to remove the dissolved gases. H_2 production using commercial CdS_c and Pt@CdS_c was then analysed by direct injection of gases collected from the headspace (16 mL) using a gas-tight syringe (injection volume of 250 μL) into the gas chromatograph. The Pt@CdS_c showed a low H_2 production rate (0.214 mmol g^{-1} h^{-1}) (Figure 1c, and Figure S6). The observed H_2 production results using Cd-SSs, Cd-Pt_2-SSs, and Pt@CdS_c were further compared with previously reported photocatalytic H_2 production activity values of Pt-CdS^R in Figure 1c.[25] It can be seen from Figure 1c that the Cd-Pt_2-SSs reaction suspension demonstrated 723 times higher solar H_2 production than that of Pt@CdS_c (0.214 mmol g^{-1} h^{-1}), and 736 times higher than the previously reported Pt-CdS^R nanoparticulate systems (0.21 mmol g^{-1} h^{-1}).[25] Furthermore, even without using Pt, the Cd-SSs suspension produced 154 and 157-fold higher H_2 production rates than the Pt@CdS_c and Pt-CdS^R nanoparticles[25] (Figure 1c, Note S1), respectively. The real-time optical images of the solvent (SSs), single metal precursor suspensions (Cd-SSs), and Cd-Pt_2-SSs reaction suspension before and after photoirradiation are shown in Figure S7.

We checked the influence of the excitation wavelength on H_2 production using the Cd-Pt_2-SSs reaction suspension for 4 different cut-off wavelengths (Figure 1d). These results firmly supported the operational viability under visible light illumination. The recorded video (Movie S1) highlighted the release of H_2 bubbles from the settled down Cd-Pt_2-SSs reaction suspension in a glass test tube on irradiation with 365 nm LED light. The solar H_2-production rates of the Cd-Pt_2-SSs reaction suspension under UV/Visible light irradiation can be well maintained during repeated (Figure 1e) and long-term (Figure S8) stability tests. The relatively small decrease in H_2 production during the photocatalytic cycles is

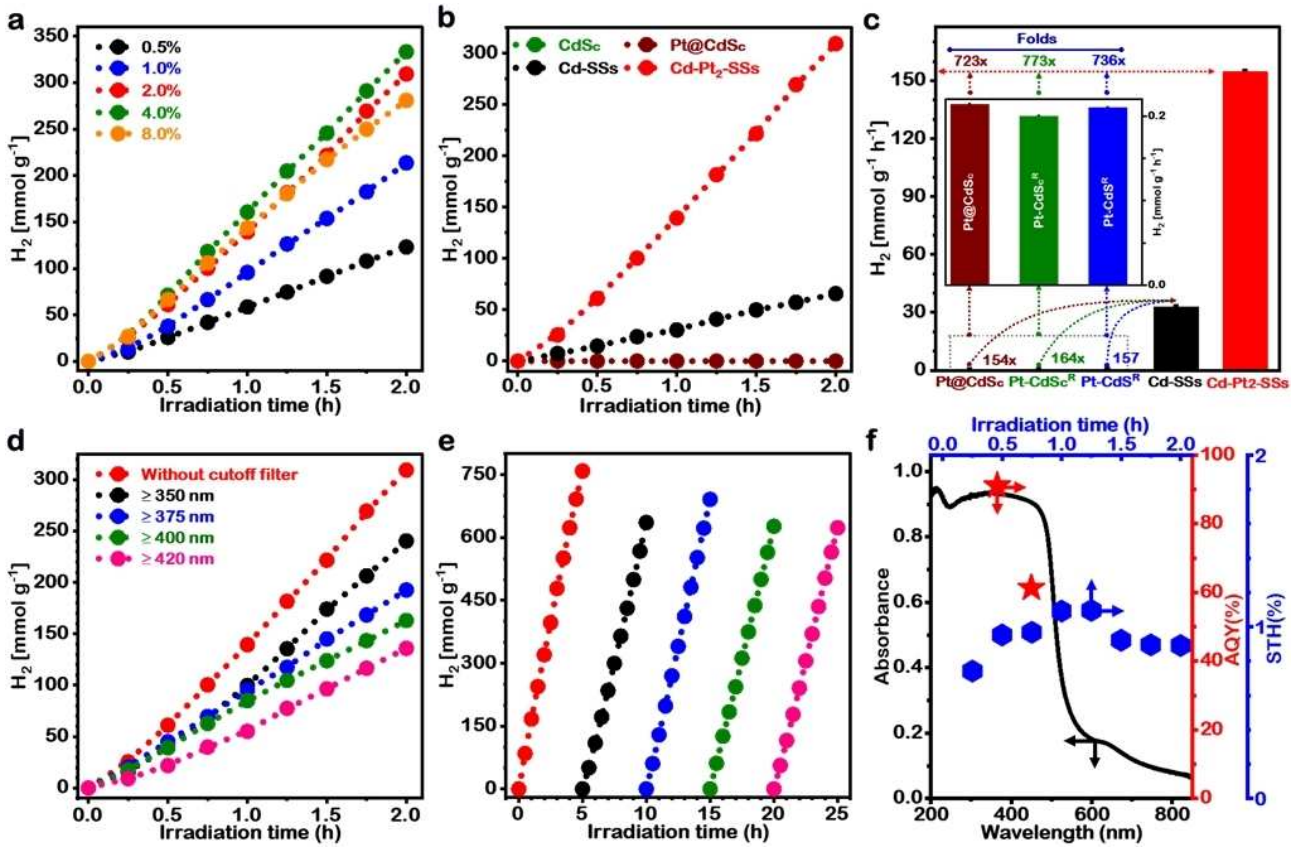

Figure 1. Photochemical H_2 production performance of Cd_x-Pt_y-SSs. a, H_2 production time profile for mixed metals precursors suspension, Cd_x-Pt_y-SSs (x = 1 mg in 15 mL SSs, y = 0.5 to 8.0 wt.% Pt of x). b, Comparison of H_2 production time profiles of Cd-SSs and Cd-Pt_2-SSs with commercial CdS_c and 2%Pt@CdS_c. (Note: H_2 production profile of commercial 2%Pt@CdS_c overlaps with that of CdS_c). c, H_2 production rate over commercial CdS_c (this study), commercial CdS reported in the referred paper (CdS_c^R), and CdS nanoparticles (CdS^R) reported by Bag et al.[25] (inset magnified bar graph), and a comparison with Cd-SSs and Cd-Pt_2-SSs reaction suspension. d, Time profile of H_2 production from Cd-Pt_2-SSs at different cut-off wavelengths. e, Repeated run stability analysis of Cd-Pt_2-SSs. f, Apparent quantum yield as a function of the incident light wavelength, and time profile of solar to hydrogen conversion efficiency ($2H^+ + 2e^- \rightarrow H_2$).

probably due to modifications in the nearby coordination environments of active sites and some structural changes in the photocatalysts. The stability of the solid material collected from Cd-Pt_2-SSs reaction suspension after the 5th run of cyclic stability test has been analysed by UV/Vis absorbance (Figure S9), Raman (Figure S10), Fourier transform infrared (FTIR) (Figure S11), and N_2 adsorption-desorption (Figure S12) analyses. All these studies further confirm the structural stability of the photocatalytic system. Also, to check the possibility of any photo-chemical corrosion of in situ generated Pt_{SA}-CdS_{IS}, microwave plasma-atomic emission spectroscopy (MP-AES) (Figures S13 and S14) has been used; however, the obtained results indicate the complete absence of Cd and Pt in the solution phase. A high AQY (≈91.1 % (365 nm), and 61.3 % (450 nm)), and solar-to-hydrogen conversion efficiency, (η ≈1.0 %) were achieved in the presence of an electron donor (Figure 1f).

The reaction suspensions (Cd-Pt_2-SSs and Cd-SSs) used in the present study were compared with H_2 generating photocatalysts (co-catalyst loaded metal oxide, metal sulphide, carbon-based, metal–organic framework (MOF) based, and MOF-metal-carbon (MOF-M-C) photocatalysts) discussed in previous work (Table S1).[21,26–30] Our reported suspensions, which do not require any pre-synthesis, show comparable H_2 production to the previously reported photocatalysts, which require a multistep synthesis process, high-cost organic solvents, sophisticated reaction setup, additional thermal treatments, and co-catalyst loading. We note that even the Pt-free, Cd-SSs reaction suspension showed remarkable H_2 production that is comparable to that of single-atom metal catalyst loaded TiO_2, CdS, and g-C_3N_4 photocatalysts. In short, the direct use of metal precursor solutions may prove to be a novel, promising, environmentally benign, and cost-effective strategy for effective H_2 production.

Several studies have reported the effect of solar radiation on the surface structure of photocatalysts during photochemical reactions.[31–34] To explore the driving force behind the exceptional photochemical H_2 production performances of Cd-SSs and Cd-Pt_2-SSs suspensions, the chemical, electrochemical, optical, electronic, and structural characteristics of the suspended nanoparticles generated during solar H_2 production were extensively investigated. X-

ray diffraction (Figure S15) and high-angle annular dark-field scanning transmission electron microscopy (HAADF-STEM) (Figure 2a–c and Figure S16) indicated a mixture of the zincblende and wurtzite structures for in situ synthesized CdS_{IS} nanoparticles in Cd-SSs suspension by photoirradiation during solar H_2 production. Fourier transforms of the data taken from two different nanoparticles in Figure 2a demonstrate the presence of both wurtzite and zincblende structures in close proximity.

As discussed earlier, the addition of a small weight percentage of the Pt precursor (2 wt.% of Cd) to the Cd-SSs suspension results in a nearly 4.7 fold higher H_2 production than the H_2 production from the Cd-SSs suspension without Pt (Figure S4). We examined the Cd-Pt_2-SSs suspension after solar H_2 production to determine the nature of Pt in the system. HAADF-STEM images (Figure 2d and Figure S17) demonstrated the in situ formation of isolated Pt single-atoms anchored on the CdS nanoparticles (Pt_{SA}-CdS_{IS}) without any noticeable atom assemblies (two-dimensional "rafts" of Pt atoms) after solar H_2 production. However, elemental mapping using energy dispersive X-ray (EDX) spectroscopy found the presence of small nanoparticles of Pt, in addition to the single atoms (Figure 2e–h). Pt could be observed on Cd-Pt_2-SSs in regions without

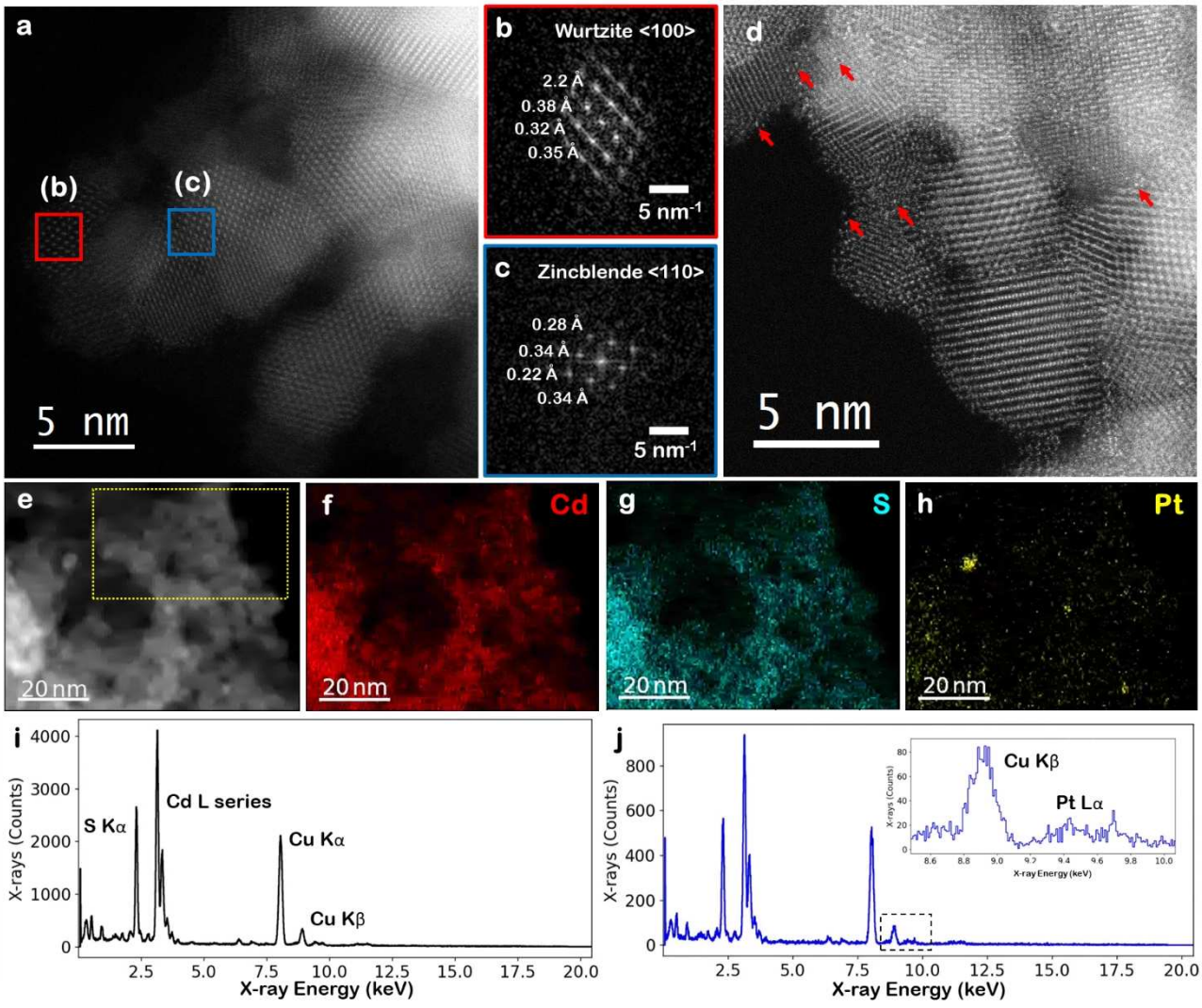

Figure 2. Structural evolution of photoinduced in situ synthesised Pt single-atoms anchored CdS_{IS} semiconductor. a, HAADF-STEM image demonstrating the atomic structure of CdS_{IS} particles. b, The Fourier Transform of the region indicated in (a), which is indexed to a <100> direction in wurtzite CdS. c, The Fourier Transform of the region indicated in (a), which is indexed to a <110> direction in zincblende CdS. d, HAADF-STEM image in which bright atoms (Pt) can be observed in addition to CdS_{IS} particles. A selection of bright atoms has been highlighted with red arrows. e, HAADF-STEM image of a region corresponding to the EDX maps in f–h, where the dashed yellow box indicates the region in which spectrum j has been extracted. f–h, Corresponding EDX maps of the full region for Cd (f), S (g), and Pt (h). Small Pt single-atom clusters can be observed in the Pt map. i, Sum EDX spectrum taken from the whole region shown in Figure 2e. Clear Cd and S peaks can be seen. j, EDX spectrum taken solely from the region highlighted in yellow dotted rectangle Figure 2e, in which there are no clear Pt nanoparticles. All peaks remain, including the Pt L peaks. Inset is a highlighted region of the spectrum specifically highlighting the presence of a small Pt Lα peak at 9.44 keV.

visible nanoparticles (Figure 2j), confirming the presence of single atoms or small clusters, which we suggest are single atoms based on the HAADF-STEM imaging conducted. On the other hand, the Cd-SSs suspension with 8 wt.% Pt showed the presence of Pt atom assemblies, along with well distributed Pt single-atoms on the CdS nanoparticles in the Cd-Pt_8-SSs suspension after solar H_2 production (Figure S18). The observed decrease in the H_2 production rate (Figure S4) for the Cd-Pt_8-SSs suspension can be expected because high Pt loading (8 wt.%) on CdS_{IS} nanoparticles can limit the radiation exposure of the CdS_{IS} nanoparticles and diminish the surface sites for the adsorption of the sacrificial agent (SSs).[35] Thus, we have achieved the in situ synthesis of isolated Pt single-atom anchored CdS nanoparticles (Pt_{SA}-CdS_{IS}) without requiring any separate synthesis process. More importantly, loading single-atom metal co-catalysts higher than 0.5 wt.% is very challenging and typically requires a complex synthesis process;[26,36–39] our approach yielded a highly dispersed distribution of Pt single-atoms anchored on CdS_{IS} along with solar H_2 production. A high atomic dispersion of Pt single-atoms anchored on CdS_{IS} nanoparticles offers robust catalytic activity, unique selectivity, and effective photoactive charge carrier utilization for photochemical H_2 production.[40]

Ex situ X-ray photoelectron spectroscopy (XPS) analysis was performed to determine the surface chemical composition and oxidation states of Cd and Pt in powder samples collected from Cd_x-Pt_y-SSs (x = 1 mg 15 mL^{-1}, y = 0, 2, 4 and 8 % of x) suspensions before and after solar H_2 production. The spectra of samples collected from Cd-Pt_2-SSs suspensions before photoirradiation showed the presence of Cd 3d and S 2p only (Figure S19). However, the spectra of powder samples collected from Cd-Pt_y-SSs suspensions after photoirradiation exhibit the presence of Cd 3d, S 2p, and Pt 4f signals (Figures 3a–d, S20–S22, and Tables S2–S4). These results demonstrate that simultaneous in situ photodeposition of Pt does not occur without UV/Visible light irradiation. In fact, it confirms the facile synthesis of a photoinduced Pt_{SA}-CdS_{IS} (Figures 2a, 3d, S17, S18, S21, S22)

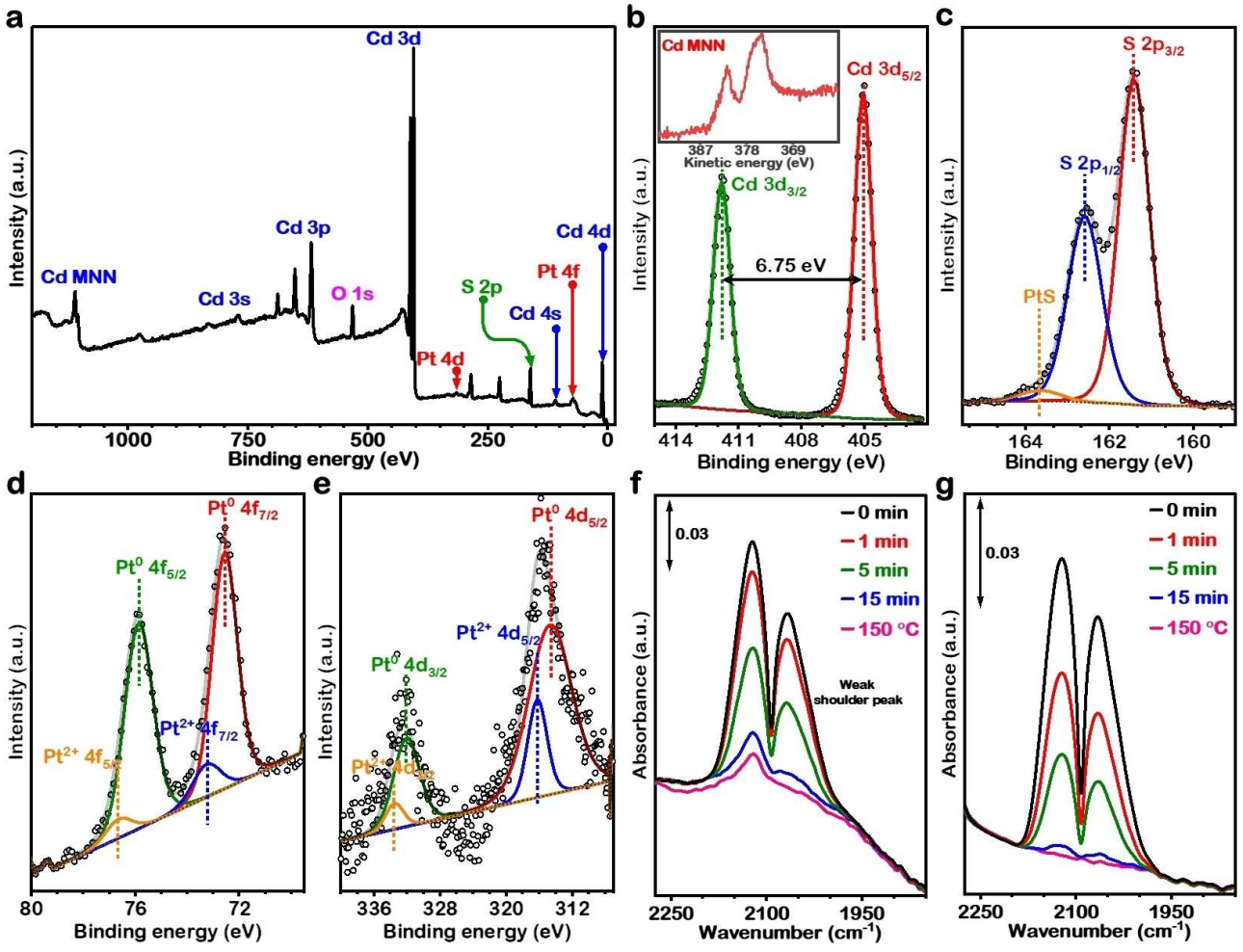

Figure 3. Electronic state identification of atomically dispersed Pt atoms over an in situ generated Pt_{SA}-CdS_{IS} photocatalyst. a, Overall XPS survey spectrum of Pt_{SA}-CdS_{IS} (2 wt.%Pt of Cd). b, High-resolution XPS spectra of Cd 3d, Cd MNN (inset spectrum) and c, S 2p for Pt_{SA}-CdS_{IS} photocatalyst. Deconvolution of the high-resolution XPS peaks for d, Pt 4f and e, Pt 4d showing the presence of Pt^0 single atoms. Time-dependent FTIR spectra of CO adsorbed at 293 K (0 min) followed by desorption using He gas purging (20 cc min^{-1}) and thermal treatment at 150 °C, 30 min for f, Pt_{SA}-CdS_{IS} and g, commercial 5 %Pt/Al_2O_3 samples.

alongside H_2 production (Figure 1) from Cd-Pt_y-SSs suspensions.

The high-resolution X-ray photoemission spectrum of the Cd 3d peaks (Figure 3b) showed Cd $3d_{3/2}$ (411.7 eV) and Cd $3d_{5/2}$ (405.0 eV) peaks, which correspond to the characteristic peak of the Cd^{2+} oxidation state of CdS_{IS}. The characteristic binding energies states of S $2p_{1/2}$ (162.5 eV) and S $2p_{3/2}$ (161.4 eV) are determined by deconvoluting them from the main S 2p peak in Figure 3c. The observed peaks of the S 2p states confirm the presence of S^{2-} in the Pt_{SA}-CdS_{IS}.

The high-resolution XPS spectra for Pt 4f (Figure 3d) indicated two kinds of platinum species[41] with a small change in the binding energies of Pt $4f_{7/2}$ and Pt $4f_{5/2}$.[42] Deconvolution analysis revealed the peaks at 72.3 and 75.6 eV with a spin-orbit split of 3.3 eV, indicating the presence of Pt^0, while the peaks at 73.4 and 76.7 eV can be assigned to Pt^{2+}.[43,44] The higher Pt^0 binding energy in Pt_{SA}-CdS_{IS} (72.3 eV) than the standard 71.8 eV suggests stronger electronic interaction between Pt_{SA} and CdS_{IS}. The presence of the well-contacted interface between Pt_{SA} and CdS_{IS} enhances electron mobility across the interface and reduces the energy barriers for H_2 evolution.[45,46]

The atomic ratio Pt^0:Pt^{2+} was estimated to be high, with Pt largely dispersed as single-atom species in the in situ synthesized Pt_{SA}-CdS_{IS} photocatalyst irrespective of initial Pt content (Tables S2–S4). Furthermore, the deconvolution of Pt 4d XPS peaks also confirms the predominance of charge-neutral Pt in the Pt_{SA}-CdS_{IS} photocatalyst (Figure 3e).[47]

Site-specific analysis using CO adsorption infrared spectroscopy (Figures 3f, and 3 g) was performed to supplement the HAADF-STEM and XPS results and to provide complementary information about the distribution of metallic platinum and the presence of Pt^0 state in the Pt_{SA}-CdS_{IS} sample. The IR absorbance spectra of adsorbed CO on Pt_{SA}-CdS_{IS} showed two strong vibration bands and a weak shoulder peak (Figure 3f). These peaks probably originate from CO molecules adsorbed on different metal species.[48–50] Furthermore, 5 wt.% metallic Pt loaded Al_2O_3 (5 %Pt/Al_2O_3) was used as a reference CO adsorption study. The CO adsorption IR spectra for commercial 5 %Pt/Al_2O_3 (Figure 3g) are similar to that of Pt_{SA}-CdS_{IS}, and are the subject of further studies.

The electronic and coordination structures of Pt species in Pt_{SA}-CdS_{IS} photocatalyst were further validated by X-ray absorption near-edge structure (XANES) and extended X-ray absorption fine structure (EXAFS) analysis in comparison to Pt foil and PtO_2 references. The normalised XANES spectra reported in Figure 4a show that white line edge intensity of Pt species in Pt_{SA}-CdS_{IS} is much lower than that of PtO_2 (Pt^{4+}) and very close to the Pt foil (Pt^0) reference, which confirms the existence of Pt species as single atoms in the in situ generated Pt_{SA}-CdS_{IS} photocatalyst, which is consistent with the HAADF-STEM (Figure 2), XPS (Figure 3a–e), and site-specific CO adsorption FTIR (Fig-

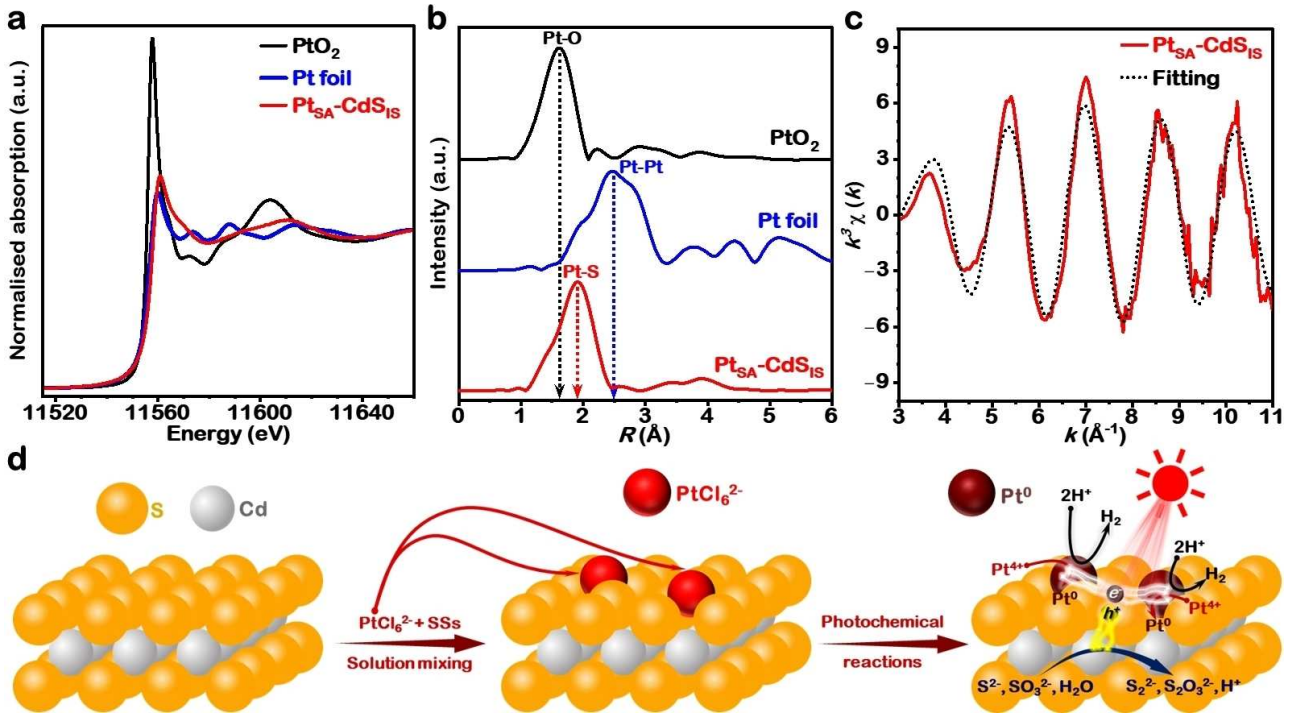

Figure 4. X-ray absorption fine structure (XAFS) measurement of Pt_{SA}-CdS_{IS}. a, Normalised XANES spectra of Pt_{SA}-CdS_{IS}, and reference samples (PtO_2 and Pt foil) at the Pt L_3 edge. b, Fourier transformed (FT) k^3-weighted $\chi(k)$ function of the EXAFS spectra of Pt_{SA}-CdS_{IS}, PtO_2 and Pt foil. c, Corresponding EXAFS fitting curve of Pt_{SA}-CdS_{IS} at *k*. d, Possible photochemical parallel reduction reactions resulting in H_2 production and synthesis of Pt single-atom decorated CdS_{IS} semiconductor. The electron charge sharing helps in high H_2 production and high yield of single atom Pt^0.

ure 3f,g) results. As shown in Figure 4b, the presence of a prominent peak at 1.91 Å attributed to the Pt–S coordination[49,51,52] and the absence of Pt–O (≈1.63 Å) and Pt–Pt coordination (≈2.5–2.8 Å) peaks in the EXAFS spectrum of Pt_{SA}-CdS_{IS}, and the corresponding best-fitting to the data (Figure 4c) reinforce the conclusion that Pt remained atomically dispersed on in situ generated CdS_{IS}.[51–54] Thus, Figure 4d illustrates the occurrence of two parallel reactions: H_2 production and in situ formation of Pt single-atoms anchored CdS nanoparticles (Pt_{SA}-CdS_{IS}).

The UV–Vis absorbance spectra of the photoinduced in situ generated CdS_{IS}, and Pt_{SA}-CdS_{IS} are reported in Figure 5a. We find that both the samples exhibited significant light absorption in the visible-light region. A small absorption band in the visible light region (550–700 nm) for Pt_{SA}-CdS_{IS} can be attributed to H_2 evolving platinum species. The band-gap energies (E_{BG}) calculated using the Kubelka–Munk function, $(F(R)h\nu)^2 = h\nu$, (Figure 5a inset) for Pt_{SA}-CdS_{IS} (2.43 eV) and CdS_{IS} (2.46 eV) are relatively similar and confirm that they can act as visible light absorbing photocatalysts.

The photochemical performance of a photocatalyst also depends on the conduction band (CB) and valence band (VB) positions, which were calculated following the method

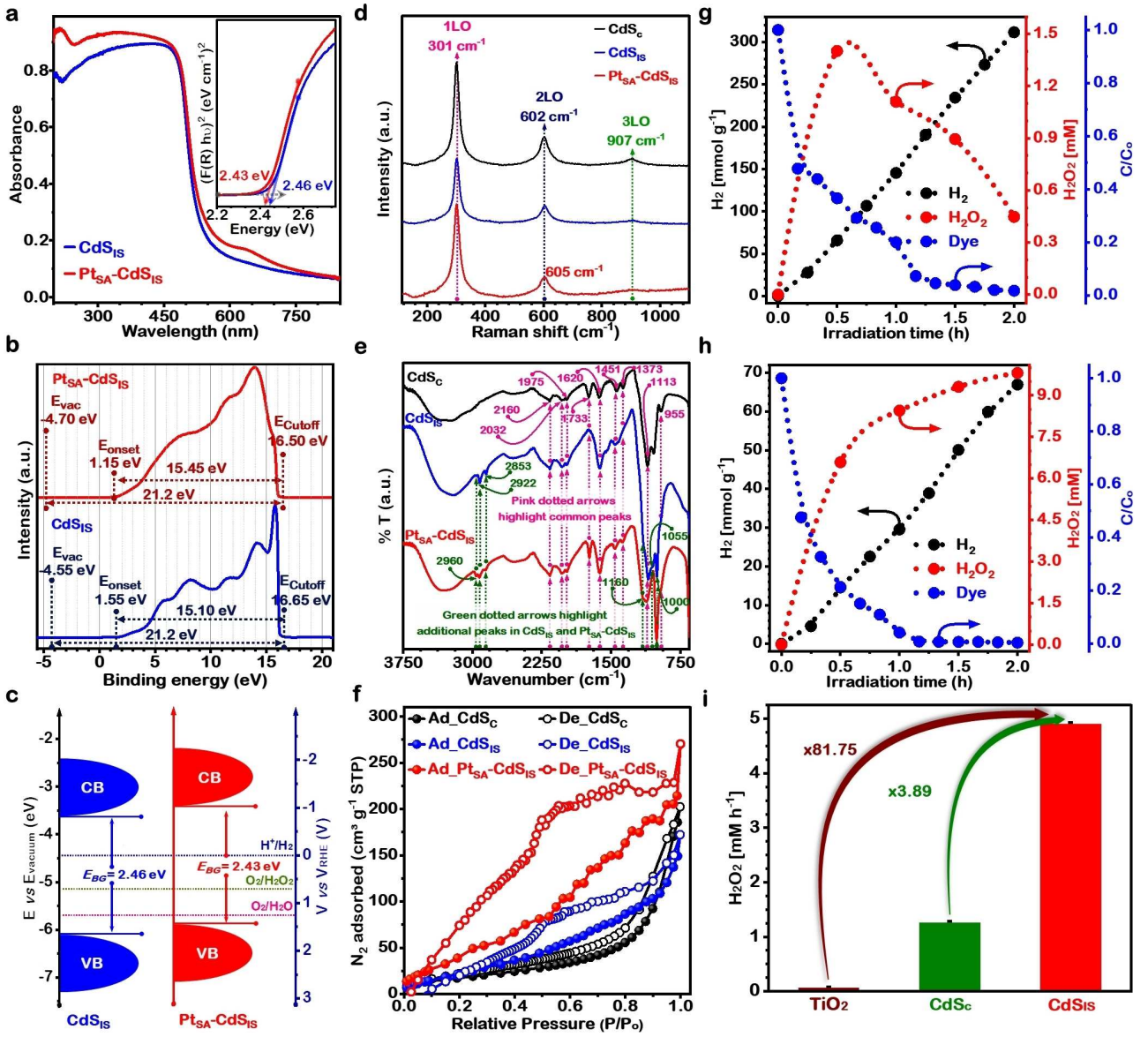

Figure 5. Electronic, physiochemical, and photochemical analysis of in situ generated Pt_{SA}-CdS_{IS} and CdS_{IS}. a, Solid-state UV/Vis absorbance spectra and Kubelka–Munk plot (inset) for the band gap calculation. b, UPS spectra of CdS_{IS}, and Pt_{SA}-CdS_{IS}. c, Schematic of band gap and energy level bands with respect to vacuum level and reversible hydrogen electrode (RHE). d, Raman spectra, e, ATR-FTIR spectra, and f, N_2 adsorption-desorption isotherms for CdS_{IS} and Pt_{SA}-CdS_{IS} photocatalysts. Solar H_2 production, O_2 reduction to H_2O_2, and dye degradation performance of g, Pt_{SA}-CdS_{IS} and h, CdS_{IS}. i, A comparison of H_2O_2 production rate over commercial CdS (CdS_C, 98% Alfa Aesar), commercial TiO_2, and as-synthesized CdS_{IS} nanoparticles.

reported by Liu et al..[14] The valence band maximum for the respective photocatalysts was calculated by estimating the ionization potential (equivalent to the valence band energy (E_{VB})) by subtracting the width of the He I UPS spectrum (Figure 5b) from the excitation energy (21.2 eV). The relative E_{VB} are calculated to be −6.10 eV (CdS_{IS}) and −5.85 eV (Pt_{SA}-CdS_{IS}) compared with E_{vacuum} according to UPS spectra (Figure 5b and c). Using the E_{BG} values the CB edge/energy (E_{CB}) of CdS_{IS} and Pt_{SA}-CdS_{IS} have been estimated to be −3.64 eV, and −3.42 eV, respectively (Figure 5c).

Raman (Figure 5d) and FTIR (Figure 5e) spectra confirmed the in situ crystallization of CdS_{IS}. Raman spectra, as presented in Figure 5d, reveal the strongest peaks at 301 cm^{-1}, which is due to first-order longitudinal optical (LO) phonons, and second-order LO (2LO) occurring at ≈602 cm^{-1} identified as characteristic peaks for CdS.[55] In comparison with CdS_{IS}, these peaks are relatively intense for Pt_{SA}-CdS_{IS}, suggesting possible electric field enhancement over the CdS_{IS} surface.[56] The photoluminescence (PL) emission spectra for CdS_c, CdS_{IS}, and Pt_{SA}-CdS_{IS} recorded at an excitation wavelength of 450 nm (Figure S23) provide information about the effective separation of photogenerated charge carriers. Figure S23 highlights the suppressed electron-hole pair recombination rate and enhanced charge carrier separation efficiency of CdS_{IS}, and Pt_{SA}-CdS_{IS} relative to commercial CdS_c.

To explore the textural properties, and to study the porous character of CdS_{IS} and Pt_{SA}-CdS_{IS} nanoparticles, N_2 adsorption-desorption measurements were performed at 77 K (Figure 5f, and Table S5). Furthermore, a comparison of the textural properties of Pt_{SA}-CdS_{IS} nanoparticles with commercial CdS_c (Figure 5f, Table S5) highlights a larger BET-specific surface area (S_{BET}) of 151.3 $m^2 g^{-1}$ owing to the nanostructure of CdS_{IS}, the relatively higher porosity/mesoporous character, and atomically decorated Pt_{SA}, whereas the CdS_c particles have a lower S_{BET} (62.85 $m^2 g^{-1}$). The nanostructure of Pt_{SA}-CdS_{IS} which arises from the photoinduced controlled crystallization might contribute to the improved surface structure and light-harvesting efficiency.

The photochemical performance of both in situ generated visible-light absorbers has been comprehensively investigated under UV/Visible light for H_2 evolution, H_2O_2 production, and dye degradation (Figures 5g, 5 h and Figures S24 and S25). The H_2 and H_2O_2 production profiles, and alizarin red S (ARS) dye degradation over time for Pt_{SA}-CdS_{IS} and CdS_{IS} photocatalysts are reported in Figure 5g and Figure 5h, respectively. As expected, the solar H_2 production over these two photocatalysts Pt_{SA}-CdS_{IS} and CdS_{IS} is similar to the photochemical H_2 production performance of their mother liquids Cd-Pt_2-SSs and Cd-SSs, respectively. Interestingly, a record high solar H_2O_2 production of 4.91 $mM h^{-1}$ was recorded for CdS_{IS} in O_2 saturated 10 M ethanol solution (Figure 5h). In contrast, commercial CdS_c (Figure S26) and TiO_2 (Figure S27) photocatalysts show low solar H_2O_2 production under the same experimental conditions compared to that of CdS_{IS} (Figure 5i). Furthermore, a comparison was made with previously reported photocatalysts for similar reaction systems, and CdS_{IS} shows a comparable solar H_2O_2 production rate (Table S6).

In this study, we report the successful synthesis of transparent Pt_{SA}-CdS_{IS} and CdS_{IS} films having exceptional photocatalytic activity and good PEC performance. Pt_{SA}-CdS_{IS}, CdS_{IS}, and CdS_c films were fabricated by a simple drop-casting method on a fluorine-doped tin oxide (FTO) glass substrate and were subsequently dried at room temperature followed by vacuum drying. The top view SEM images (Figures 6a, and b) and digital photographs (inset images) of the Pt_{SA}-CdS_{IS} and CdS_{IS} films demonstrate a uniform and transparent film formation on the FTO substrate.

To investigate the interfacial charge separation and transport behaviour of the samples (Pt_{SA}-CdS_{IS}, CdS_{IS} and CdS_c), electrochemical impedance spectroscopy (EIS) measurements were conducted under light irradiation and dark conditions. Nyquist plots shown in Figure 6c demonstrated that a smaller arc radius was observed for Pt_{SA}-CdS_{IS} both in the dark and under illumination as compared to those of CdS_{IS} and CdS_c. As arcs in the Nyquist plot reflect charge-transfer resistance at the electrode surface, so a smaller arc radius indicates a fast interfacial charge transfer and an effective separation of the photogenerated electron–hole pairs in Pt_{SA}-CdS_{IS}. Furthermore, the photocurrent density-potential profiles shown in Figure 6d demonstrated the PEC performance of Pt_{SA}-CdS_{IS}, CdS_{IS} and CdS_c photoanode from water oxidation via front illumination. These results clearly show a higher photocurrent response for Pt_{SA}-CdS_{IS} which complements the EIS results that a reduction in recombination of electron-hole pairs increases electron mobility.

To provide further information about the kinetics and electron transfer number (n) involved in the oxygen reduction reaction for H_2O_2 production (Figure 5h**)**, we performed linear sweep voltammetry (LSV) experiments in oxygen saturated 0.1 M KOH solution (Figure 6e, and Figure S28a, and S29a). The current curves of the steady-state diffusion platform analyzed by the Koutecky–Levich (K–L) equation and the linearly fitted K–L plots for CdS_{IS}, Pt_{SA}-CdS_{IS} and CdS_c are reported in Figure 6f, Figures S28b, and S29b, respectively. The slope of these K–L plots was utilised to evaluate the overall electron transfer number for the ORR. The estimated electron participation in ORR corresponding to different potentials in Figure 6g shows that the average value of n is 1.96 for CdS_{IS}, confirming the selective two-electron ORR pathway to the H_2O_2 production over its surface.

Conclusion

In contrast to the usual requirement of pre-synthesized photocatalysts for H_2 production, we have demonstrated a proof-of-concept involving the direct use of metal (Cd and Pt) precursors in (sodium sulphide + sodium sulphite) solution as a UV/Visible light photocatalytic system and achieved significant photocatalytic H_2 production activity (154.7 $mmol g^{-1} h^{-1}$ Cd-Pt_2-SSs), with an apparent quantum

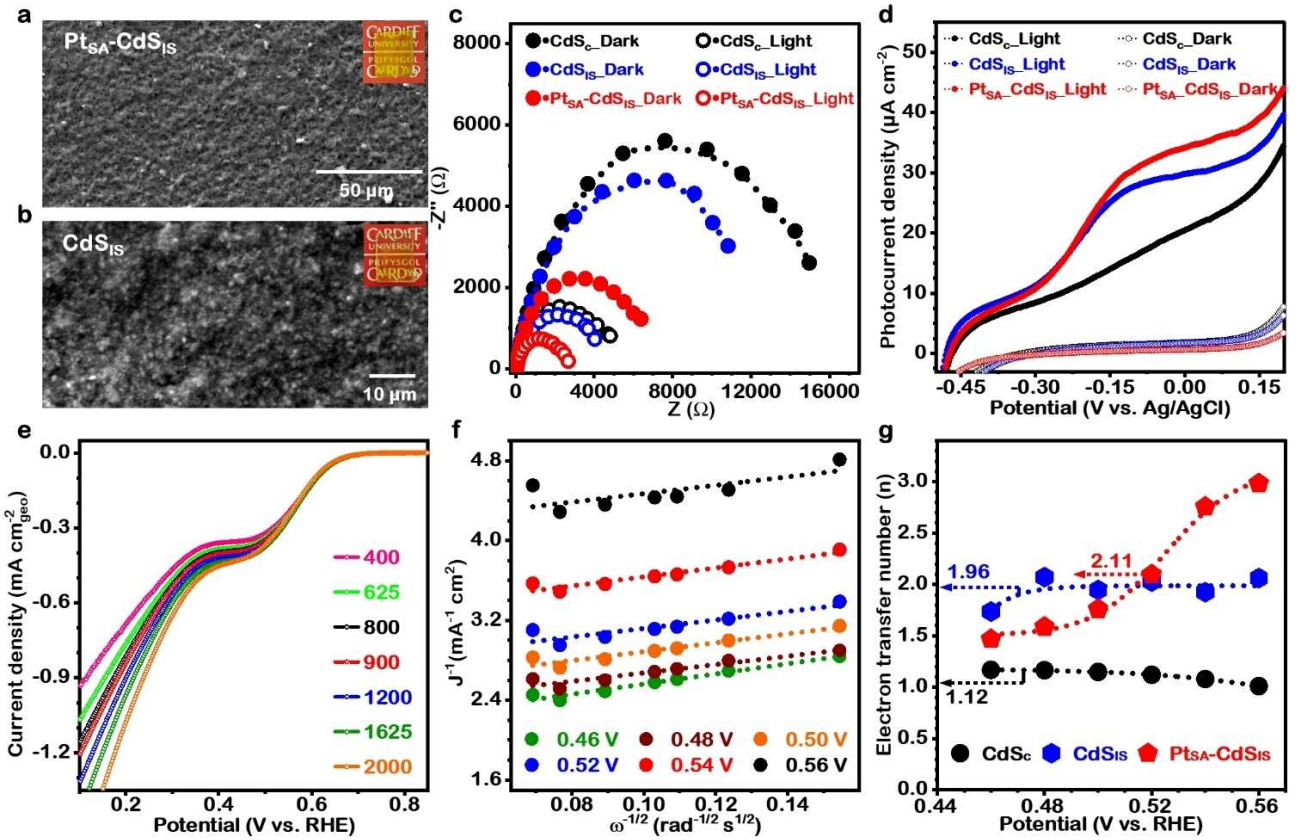

Figure 6. Photo-electrochemical performance. Top-view SEM image of drop cast a, Pt_{SA}-CdS_{IS} and b, CdS_{IS} film on conductive FTO substrate. Inset digital photographs highlight the transparency of photoanodes. c, EIS Nyquist plots, and d, Photocurrent density-potential profile of Pt_{SA}-CdS_{IS}, CdS_{IS}, and CdS_c. e, Linear sweep voltammetry (LSV) of CdS_{IS} in O_2 saturated 0.1 M KOH (pH 13) at different rotating speeds ranging from 400–2500 rpm and a fixed scanning rate of 5 mV s^{-1}. f, Koutecky–Levich (K–L) plots of CdS_{IS} at different potentials. g, The evaluated number of electrons participating in the ORR at corresponding potentials for CdS_c, CdS_{IS}, and Pt_{SA}-CdS_{IS} photocatalysts.

yield of over 91 % which outperforms previously reported photochemical particulate systems. More importantly, we have observed simultaneous photoinduced in situ synthesis of Pt single-atom anchored on CdS nanoparticles (Pt_{SA}-CdS_{IS}) without utilizing any functionalized organic solvents. We suggest the junction formed between Pt_{SA} and CdS_{IS}, and the excellent H_2 activation property of Pt are responsible for the enhanced photocatalytic activity. So, the synergistic roles of Pt and CdS lead to it being more favourable for transferring photoexcited electrons (e^-) to Pt, while Pt_{SA} ensures outstanding e^- mobility and offers more active sites for reducing H^+ to H_2. The present work provides a promising, economical, and green strategy for H_2 production along with the synthesis of metal-semiconductor heterostructures, and offers an alternative approach to solar H_2 production and catalyst synthesis. Furthermore, preliminary studies show that this strategy of the direct use of precursor suspensions can be applied to other metal systems and sulphide semiconductors, and will be discussed in more detail in future work.

Acknowledgements

This research has been supported and funded by European Union's Horizon 2020 research and innovation programme under the Marie Skłodowska-Curie grant agreement No. 892213-USHPP to P.S. We acknowledge Prof. Michael Bowker for his advice and support. We thank Diamond Light Source for access and support in the use of the electron Physical Science Imaging Centre (Instrument E01 and E02 and proposal number MG31082) that contributed to the results presented here. The X-ray photoelectron (XPS) data collection was performed at the EPSRC National Facility for XPS ("HarwellXPS"), operated by Cardiff University and UCL, under Contract No. PR16195. We are grateful for support from the UK Catalysis Hub which is funded by EPSRC grant: EP/R026939/1, EP/R026815/1, EP/R026645/1, EP/R027129/1. Access to the XAS beamline was provided through the UK Catalysis Hub Block Allocation Group (BAG), allocation SP29271-5. We thank the Research Complex, Central Laser Facility, Science and Technology Facilities Council (STFC) for access to their facilities and equipment. We thank Dr. Ajay Jha for his help in the Raman spectroscopy measurement.

Conflict of Interest

The authors declare no conflict of interest.

Data Availability Statement

The data that support the findings of this study are available in the supplementary material of this article.

Keywords: Hydrogen Production · Photocatalysis · Photocatalyst Synthesis Free · Solar Energy Assisted Material Synthesis · in Situ Single Atom Pt Decorated CdS (Pt_{SA}-CdS_{IS}) Synthesis

[1] Q. Wang, K. Domen, *Chem. Rev.* **2020**, *120*, 919–985.
[2] J. L. White, M. F. Baruch, J. E. Pander, Y. Hu, I. C. Fortmeyer, J. E. Park, T. Zhang, K. Liao, J. Gu, Y. Yan, T. W. Shaw, E. Abelev, A. B. Bocarsly, *Chem. Rev.* **2015**, *115*, 12888–12935.
[3] M. Ko, Y. Kim, J. Woo, B. Lee, R. Mehrotra, P. Sharma, J. Kim, S. W. Hwang, H. Y. Jeong, H. Lim, S. H. Joo, J. W. Jang, J. H. Kwak, *Nat. Catal.* **2022**, *5*, 37–44.
[4] H. Hou, X. Zeng, X. Zhang, *Angew. Chem. Int. Ed.* **2020**, *59*, 17356–17376; *Angew. Chem.* **2020**, *132*, 17508–17529.
[5] J. H. Kim, D. Hansora, P. Sharma, J.-W. Jang, J. S. Lee, *Chem. Soc. Rev.* **2019**, *48*, 1908–1971.
[6] A. Fujishima, K. Honda, *Nature* **1972**, *238*, 37–38.
[7] T. Takata, J. Jiang, Y. Sakata, M. Nakabayashi, N. Shibata, V. Nandal, K. Seki, T. Hisatomi, K. Domen, *Nature* **2020**, *581*, 411–414.
[8] H. Nishiyama, T. Yamada, M. Nakabayashi, Y. Maehara, M. Yamaguchi, Y. Kuromiya, Y. Nagatsuma, H. Tokudome, S. Akiyama, T. Watanabe, R. Narushima, S. Okunaka, N. Shibata, T. Takata, T. Hisatomi, K. Domen, *Nature* **2021**, *598*, 304–307.
[9] P. Sharma, T. J. A. Slater, M. Sharma, M. Bowker, C. R. A. Catlow, *Chem. Mater.* **2022**, *34*, 5511–5521.
[10] C. M. Wolff, P. D. Frischmann, M. Schulze, B. J. Bohn, R. Wein, P. Livadas, M. T. Carlson, F. Jäckel, J. Feldmann, F. Würthner, J. K. Stolarczyk, *Nat. Energy* **2018**, *3*, 862–869.
[11] Y. Li, Y.-K. Peng, L. Hu, J. Zheng, D. Prabhakaran, S. Wu, T. J. Puchtler, M. Li, K.-Y. Wong, R. A. Taylor, S. C. E. Tsang, *Nat. Commun.* **2019**, *10*, 4421.
[12] Q. Wang, M. Nakabayashi, T. Hisatomi, S. Sun, S. Akiyama, Z. Wang, Z. Pan, X. Xiao, T. Watanabe, T. Yamada, N. Shibata, T. Takata, K. Domen, *Nat. Mater.* **2019**, *18*, 827–832.
[13] Q. Wang, T. Hisatomi, Q. Jia, H. Tokudome, M. Zhong, C. Wang, Z. Pan, T. Takata, M. Nakabayashi, N. Shibata, Y. Li, I. D. Sharp, A. Kudo, T. Yamada, K. Domen, *Nat. Mater.* **2016**, *15*, 611–615.
[14] J. Liu, Y. Liu, N. Liu, Y. Han, X. Zhang, H. Huang, Y. Lifshitz, S.-T. Lee, J. Zhong, Z. Kang, *Science* **2015**, *347*, 970–974.
[15] K. Iwashina, A. Iwase, Y. H. Ng, R. Amal, A. Kudo, *J. Am. Chem. Soc.* **2015**, *137*, 604–607.
[16] X. Meng, S. Wang, C. Zhang, C. Dong, R. Li, B. Li, Q. Wang, Y. Ding, *ACS Catal.* **2022**, *12*, 10115–10126.
[17] K. Wu, P. Wu, J. Zhu, C. Liu, X. Dong, J. Wu, G. Meng, K. Xu, J. Hou, Z. Liu, X. Guo, *Chem. Eng. J.* **2019**, *360*, 221–230.
[18] X. Wang, G. Liu, L. Wang, Z.-G. Chen, G. Q. M. Lu, H.-M. Cheng, *Adv. Energy Mater.* **2012**, *2*, 42–46.
[19] D. Lang, T. Shen, Q. Xiang, *ChemCatChem* **2015**, *7*, 943–951.
[20] F. M. Zhang, J. L. Sheng, Z. Di Yang, X. J. Sun, H. L. Tang, M. Lu, H. Dong, F. C. Shen, J. Liu, Y. Q. Lan, *Angew. Chem. Int. Ed.* **2018**, *57*, 12106–12110; *Angew. Chem.* **2018**, *130*, 12282–12286.
[21] R. Lin, L. Shen, Z. Ren, W. Wu, Y. Tan, H. Fu, J. Zhang, L. Wu, *Chem. Commun.* **2014**, *50*, 8533.
[22] M. Zhang, S. Nie, T. Cheng, Y. Feng, C. Zhang, L. Zheng, L. Wu, W. Hao, Y. Ding, *Nano Energy* **2021**, *90*, 106635.
[23] M. Zhang, C. Qin, W. Sun, C. Dong, J. Zhong, K. Wu, Y. Ding, *Chin. J. Catal.* **2022**, *43*, 1818–1829.
[24] Y. Hong, Y. Cho, E. M. Go, P. Sharma, H. Cho, B. Lee, S. M. Lee, S. O. Park, M. Ko, S. K. Kwak, C. Yang, J. W. Jang, *Chem. Eng. J.* **2021**, *418*, 129346.
[25] P. P. Bag, X.-S. Wang, P. Sahoo, J. Xiong, R. Cao, *Catal. Sci. Technol.* **2017**, *7*, 5113–5119.
[26] Y. Zhang, J. Zhao, H. Wang, B. Xiao, W. Zhang, X. Zhao, T. Lv, M. Thangamuthu, J. Zhang, Y. Guo, J. Ma, L. Lin, J. Tang, R. Huang, Q. Liu, *Nat. Commun.* **2022**, *13*, 58.
[27] Y. Chen, S. Ji, W. Sun, Y. Lei, Q. Wang, A. Li, W. Chen, G. Zhou, Z. Zhang, Y. Wang, L. Zheng, Q. Zhang, L. Gu, X. Han, D. Wang, Y. Li, *Angew. Chem. Int. Ed.* **2020**, *59*, 1295–1301; *Angew. Chem.* **2020**, *132*, 1311–1317.
[28] X. Wu, H. Zhang, J. Dong, M. Qiu, J. Kong, Y. Zhang, Y. Li, G. Xu, J. Zhang, J. Ye, *Nano Energy* **2018**, *45*, 109–117.
[29] Q. Han, B. Wang, J. Gao, L. Qu, *Angew. Chem. Int. Ed.* **2016**, *55*, 10849–10853; *Angew. Chem.* **2016**, *128*, 11007–11011.
[30] H. Yang, M. Zhao, J. Zhang, J. Ma, P. Wu, W. Liu, L. Wen, *J. Mater. Chem. A* **2019**, *7*, 20742–20749.
[31] S. Wang, T. He, P. Chen, A. Du, K. (Ken) Ostrikov, W. Huang, L. Wang, *Adv. Mater.* **2020**, *32*, 2001385.
[32] O. E. Dagdeviren, D. Glass, R. Sapienza, E. Cortés, S. A. Maier, I. P. Parkin, P. Grütter, R. Quesada-Cabrera, *Nano Lett.* **2021**, *21*, 8348–8354.
[33] S. Feng, T. Wang, B. Liu, C. Hu, L. Li, Z. Zhao, J. Gong, *Angew. Chem. Int. Ed.* **2020**, *59*, 2044–2048; *Angew. Chem.* **2020**, *132*, 2060–2064.
[34] T. Li, J. He, B. Peña, C. P. Berlinguette, *Angew. Chem. Int. Ed.* **2016**, *55*, 1769–1772; *Angew. Chem.* **2016**, *128*, 1801–1804.
[35] Y. P. Xie, Z. B. Yu, G. Liu, X. L. Ma, H.-M. Cheng, *Energy Environ. Sci.* **2014**, *7*, 1895.
[36] J. Resasco, L. Derita, S. Dai, J. P. Chada, M. Xu, X. Yan, J. Finzel, S. Hanukovich, A. S. Hoffman, G. W. Graham, S. R. Bare, X. Pan, P. Christopher, *J. Am. Chem. Soc.* **2020**, *142*, 169–184.
[37] X. Li, W. Bi, L. Zhang, S. Tao, W. Chu, Q. Zhang, Y. Luo, C. Wu, Y. Xie, *Adv. Mater.* **2016**, *28*, 2427–2431.
[38] Z. Teng, Q. Zhang, H. Yang, K. Kato, W. Yang, Y. R. Lu, S. Liu, C. Wang, A. Yamakata, C. Su, B. Liu, T. Ohno, *Nat. Catal.* **2021**, *4*, 374–384.
[39] Y. Zhao, H. Zhou, X. Zhu, Y. Qu, C. Xiong, Z. Xue, Q. Zhang, X. Liu, F. Zhou, X. Mou, W. Wang, M. Chen, Y. Xiong, X. Lin, Y. Lin, W. Chen, H. J. Wang, Z. Jiang, L. Zheng, T. Yao, J. Dong, S. Wei, W. Huang, L. Gu, J. Luo, Y. Li, Y. Wu, *Nat. Catal.* **2021**, *4*, 134–143.
[40] J. A. Nasir, Z. U. Rehman, S. N. A. Shah, A. Khan, I. S. Butler, C. R. A. Catlow, *J. Mater. Chem. A* **2020**, *8*, 20752–20780.
[41] C. Chen, Y. Kang, Z. Huo, Z. Zhu, W. Huang, H. L. Xin, J. D. Snyder, D. Li, J. A. Herron, M. Mavrikakis, M. Chi, K. L. More, Y. Li, N. M. Markovic, G. A. Somorjai, P. Yang, V. R. Stamenkovic, *Science* **2014**, *343*, 1339–1343.
[42] K. L. Zhou, Z. Wang, C. B. Han, X. Ke, C. Wang, Y. Jin, Q. Zhang, J. Liu, H. Wang, H. Yan, *Nat. Commun.* **2021**, *12*, 3783.
[43] Z. Liu, S. Ma, L. Chen, J. Xu, J. Ou, M. Ye, *Mater. Chem. Front.* **2019**, *3*, 851–859.
[44] P. Xie, T. Pu, A. Nie, S. Hwang, S. C. Purdy, W. Yu, D. Su, J. T. Miller, C. Wang, *ACS Catal.* **2018**, *8*, 4044–4048.
[45] Y. Shi, Z.-R. Ma, Y.-Y. Xiao, Y.-C. Yin, W.-M. Huang, Z.-C. Huang, Y.-Z. Zheng, F.-Y. Mu, R. Huang, G.-Y. Shi, Y.-Y. Sun, X.-H. Xia, W. Chen, *Nat. Commun.* **2021**, *12*, 3021.

[46] A. Z. Jovanović, L. Bijelić, A. S. Dobrota, N. V. Skorodumova, S. V. Mentus, I. A. Pašti, *Electrochim. Acta* **2022**, *414*, 140214.
[47] S. Bai, B. Huang, Q. Shao, X. Huang, *ACS Appl. Mater. Interfaces* **2018**, *10*, 22257–22263.
[48] K. Ding, A. Gulec, A. M. Johnson, N. M. Schweitzer, G. D. Stucky, L. D. Marks, P. C. Stair, *Science* **2015**, *350*, 189–192.
[49] X. Shi, C. Dai, X. Wang, J. Hu, J. Zhang, L. Zheng, L. Mao, H. Zheng, M. Zhu, *Nat. Commun.* **2022**, *13*, 1287.
[50] B. Qiao, A. Wang, X. Yang, L. F. Allard, Z. Jiang, Y. Cui, J. Liu, J. Li, T. Zhang, *Nat. Chem.* **2011**, *3*, 634–641.
[51] L. Wang, M.-X. Chen, Q.-Q. Yan, S.-L. Xu, S.-Q. Chu, P. Chen, Y. Lin, H.-W. Liang, *Sci. Adv.* **2019**, *5*, eaax6322.
[52] J. Zhu, L. Cai, X. Yin, Z. Wang, L. Zhang, H. Ma, Y. Ke, Y. Du, S. Xi, A. T. S. Wee, Y. Chai, W. Zhang, *ACS Nano* **2020**, *14*, 5600–5608.
[53] Y. Zhu, T. Cao, C. Cao, J. Luo, W. Chen, L. Zheng, J. Dong, J. Zhang, Y. Han, Z. Li, C. Chen, Q. Peng, D. Wang, Y. Li, *ACS Catal.* **2018**, *8*, 10004–10011.
[54] Q.-Q. Yan, D.-X. Wu, S.-Q. Chu, Z.-Q. Chen, Y. Lin, M.-X. Chen, J. Zhang, X.-J. Wu, H.-W. Liang, *Nat. Commun.* **2019**, *10*, 4977.
[55] C. Han, Z.-R. Tang, J. Liu, S. Jin, Y.-J. Xu, *Chem. Sci.* **2019**, *10*, 3514–3522.
[56] V. Dzhagan, A. G. Milekhin, M. Y. Valakh, S. Pedetti, M. Tessier, B. Dubertret, D. R. T. Zahn, *Nanoscale* **2016**, *8*, 17204–17212.

Manuscript received: January 24, 2023
Accepted manuscript online: February 14, 2023
Version of record online: ■■, ■■

Forschungsartikel

Photocatalytic H_2 Evolution

P. Sharma,* M. Sharma, M. Dearg, M. Wilding, T. J. A. Slater, C. R. A. Catlow* **e202301239**

Cd/Pt Precursor Solution for Solar H_2 Production and in situ Photochemical Synthesis of Pt Single-atom Decorated CdS Nanoparticles

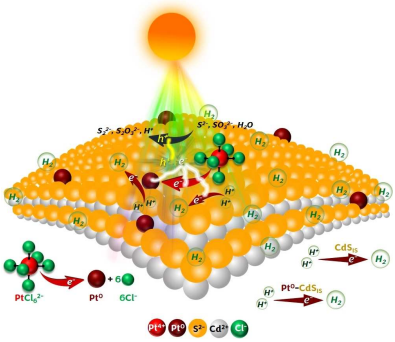

This work reports the use of Cd/Pt precursor solutions for substantially higher photocatalytic H_2 production (154.7 mmol g^{-1} h^{-1}), thereby eliminating the need for pre-synthesized photocatalysts for H_2 production. Furthermore, in parallel to H_2 production, a simplified solar light-assisted in situ synthesis of Pt single-atom anchored CdS nanoparticles (Pt_{SA}-CdS_{IS}) has also been demonstrated.